Available online at www.sciencedirect.com

ScienceDirect

Journal of Catalysis 249 (2007) 380–393

JOURNAL OF CATALYSIS

www.elsevier.com/locate/jcat

Methane catalytic partial oxidation on autothermal Rh and Pt foam catalysts: Oxidation and reforming zones, transport effects, and approach to thermodynamic equilibrium

R. Horn *, K.A. Williams, N.J. Degenstein, A. Bitsch-Larsen, D. Dalle Nogare, S.A. Tupy, L.D. Schmidt

Department of Chemical Engineering and Materials Science, University of Minnesota, 421 Washington Avenue SE, Minneapolis, MN 55455, USA

Received 7 February 2007; revised 13 April 2007; accepted 3 May 2007

Abstract

We compare Rh and Pt as catalysts for the partial oxidation of methane to syngas at millisecond contact times. The basis for the comparison are species and temperature profiles, with a spatial resolution of about 300 μm measured along the centerline of an adiabatically operated metal-coated α-Al_2O_3 foam using a capillary sampling technique with mass spectrometric species measurement. Gas temperature profiles are measured with a thermocouple. Investigated stoichiometries range from C/O = 0.6 to 2.6 at constant flow rate of 4.7 slpm and atmospheric pressure. Rh and Pt are compared with respect to (i) profile development at syngas stoichiometry, (ii) profile development at varying stoichiometries from C/O = 0.6–2.6, (iii) product selectivities and yields in the oxidation zone, (iv) contribution of partial oxidation and steam reforming to the final syngas yield, (v) mass transport limitations, and (vi) approach to thermodynamic equilibrium. Independent of C/O and metal, all profiles show an oxidation zone and a steam-reforming zone. H_2 and CO are formed in the presence of gas-phase oxygen by partial oxidation and in the absence of gas-phase oxygen by steam reforming. CO_2 reforming is not observed. At the same C/O, H_2 and CO selectivities and yields are higher in the oxidation zone on Rh than on Pt. As the C/O ratio increases, the catalyst temperature decreases and selectivities to H_2 and CO in the oxidation zone decrease. The decrease is larger on Pt than on Rh. Because Rh is also the better steam-reforming catalyst, H_2 and CO yields are generally higher on Rh than on Pt. The rate of O_2 conversion at the catalyst entrance is largely mass transport-controlled on Rh but not on Pt. In the oxidation zone on Pt, the methane CPO is kinetically controlled with a constant reaction rate. An average O_2 mass transport coefficient is calculated and compared with literature values on foam catalysts. Finally, exit species flow rates and temperatures are compared with thermodynamic calculations at constant pressure and enthalpy. Rh brings the methane oxidation close to equilibrium if $C/O \leqslant 1.0$, whereas Pt reaches equilibrium only at very high catalyst temperatures if $C/O \leqslant 0.7$. At higher C/O, deviations from equilibrium are observed mainly because steam-reforming slows, but also because water–gas shift equilibrium is not established.

Keywords: Syngas; Catalytic partial oxidation; Methane; Rhodium; Platinum; Mechanism; Spatial profiles; Mass transport; Thermodynamics

1. Introduction

The production of syngas, a mixture of CO and H_2, is of great importance in chemical industry, because syngas is the feedstock for methanol and Fischer–Tropsch synthesis. An important resource for syngas production is natural gas, which consists of 80–90% methane. Unfortunately, natural gas occurs often in remote locations, and costly transportation motivates research to transform it to syngas and finally transportable liquids right at the well head.

Conventional steam-reforming technology is not suited for decentralized syngas production, because steam reformers are large, expensive plants that cannot be scaled down for small-scale operation in a remote gas field. The catalytic partial oxidation of methane to syngas (CPO, Eq. (1)) has received considerable attention because it provides close to 100% methane conversion and >90% syngas yields in millisecond contact times

---

[*] Corresponding author.
E-mail address: rumford@gmx.de (R. Horn).

0021-9517/$ – see front matter
doi:10.1016/j.jcat.2007.05.011

[1,2] and can be conducted in comparably small reactors ideal for decentralized applications. In addition, the methane CPO supplies a H_2/CO ratio of 2/1, which is favorable for methanol or Fischer–Tropsch synthesis.

$$CH_4 + 1/2O_2 \rightarrow CO + 2H_2, \quad \Delta H_r^\circ = -36\ \mathrm{kJ\,mol^{-1}}. \tag{1}$$

Various catalysts on different supports have been reported to be active for the methane CPO. Most catalysts contain a group VIII metal as active component (e.g., Rh, Pt, Ru, Ni) on an oxide support [3]. The present work focuses on Rh and Pt on α-Al_2O_3 foam supports.

An important and open question in methane CPO research is the reaction mechanism and product development in the catalyst bed under autothermal conditions. Direct and indirect mechanisms are proposed [3]. The direct mechanism assumes that H_2 and CO are primary reaction products formed by partial oxidation in the presence of gas-phase O_2. Equation (2) ($0 \leqslant x \leqslant 2$, $0 \leqslant y \leqslant 1$) shows the direct mechanism including the competitive formation of H_2O and CO_2.

$$\begin{aligned} &CH_4 + \left(2 - \frac{x}{2} - \frac{y}{2}\right)O_2 \\ &\quad \rightarrow xH_2 + yCO + (2-x)H_2O + (1-y)CO_2. \end{aligned} \tag{2}$$

The indirect mechanism postulates a two-zone model with strongly exothermic CH_4 combustion to H_2O and CO_2 at the catalyst entrance (Eq. (3)), followed by strongly endothermic steam- and CO_2-reforming (Eqs. (4) and (5), respectively) downstream.

$$CH_4 + 2O_2 \rightarrow CO_2 + 2H_2O, \quad \Delta H_r^\circ = -803\ \mathrm{kJ\,mol^{-1}}, \tag{3}$$

$$CH_4 + H_2O \rightarrow CO + 3H_2, \quad \Delta H_r^\circ = +206\ \mathrm{kJ\,mol^{-1}}, \tag{4}$$

$$CH_4 + CO_2 \rightarrow 2CO + 2H_2, \quad \Delta H_r^\circ = +247\ \mathrm{kJ\,mol^{-1}}. \tag{5}$$

Published mechanistic studies follow essentially two approaches. One approach is to study the methane CPO under realistic conditions (i.e., high catalyst temperatures and atmospheric or elevated pressure) and compare reactor exit data with numerical simulations assuming a reaction mechanism [1,4–9]. Another approach uses well-defined isothermal low-pressure or diluted conditions different from technical applications; examples include TAP experiments in vacuum [10–12], isothermal reactor measurements [13,14], and spectroscopic studies [15]. Depending on the experimental conditions, different product development is inferred and different mechanistic conclusions are drawn. Some authors report a direct mechanism [11,12,15], some find evidence for the indirect mechanism [9,10,13,14] and others advocate for a mechanism in between [8,16].

Our approach to studying methane CPO in as close to industrial conditions as possible is to measure high-resolution (≈300 μm) species and temperature profiles along the centerline of an autothermally operated foam catalyst. Until recently [17–19], high-resolution spatial data were absent in the literature. One earlier study provided spatially resolved data by arranging discrete, Rh-coated metallic screen substrates in a stack and sampling behind each screen [16]. The resolution of this method was limited to 2 mm, however. These data were later compared by another group with numerical simulations [20], but due to the low spatial resolution, H_2 formation was attributed to steam reforming only. No H_2 formation was attributed to partial oxidation, in contrast to our high-resolution measurements showing substantial formation of H_2 in the presence of gas-phase oxygen.

It should be noted here that even though the terms "direct" and "indirect" are commonly used in the literature to discuss the mechanism of methane CPO, Eqs. (2)–(5) describe only a stoichiometrically observed product development in the catalyst bed and give no information about the elementary reaction steps occurring at the catalyst surface. For example, we show in this work that H_2 and CO are formed in the presence of gas-phase O_2 at the entrance section of the catalyst; that is, the reaction there is a partial oxidation according to Eq. (2), but that does not necessarily mean that H_2 formation is the primary event after CH_4 dissociation at the catalyst surface. It is possible that the surface hydrogen atoms H_s are involved in rapid surface reactions with oxygen surface atoms O_s (e.g., $H_s + O_s \rightleftarrows OH_s$ and $OH_s + H_s \rightleftarrows H_2O_s$) before they leave the surface either as H_2 or H_2O. In this case, the reaction would be indirect even though it follows Eq. (2). The actual surface reaction steps can not be inferred from the spatial profiles wherefore we discuss the reaction mechanism only in terms of Eqs. (2)–(5) without using the terms "direct" and "indirect."

The motivation of this work is to present and analyze high-resolution species and temperature profiles for autothermally operated Rh and Pt foam catalysts that give new insight into the reaction mechanism under technically relevant conditions. The high-resolution spatial profiles reveal that on both metals, H_2 and CO are formed partly by partial oxidation (Eq. (2)) and partly by steam reforming (Eq. (4)). CO_2 reforming (Eq. (5)) is not observed in an adiabatic reactor. High catalyst temperatures favor the formation of H_2 and CO in three different ways: (i) by increasing the H_2 and CO selectivities in the oxidation zone of the reactor ($S_{H_2}^{oz} = x/2$, $S_{CO}^{oz} = y$ in Eq. (2)), (ii) by increasing the CH_4 conversion in the oxidation zone (H_2 and CO yields in the oxidation zone increase), and (iii) by increasing the rate of steam-reforming downstream. Because Pt favors total oxidation and does not catalyze steam reforming as efficiently as Rh does, syngas yields are generally higher on Rh than on Pt.

We begin this work by analyzing conventional conversion and selectivity data at the reactor exit (Section 3.1). We then analyze high-resolution spatial profiles measured for syngas stoichiometry (C/O = 1.0, Section 3.2) and for other C/O ratios from 0.6–2.6 (Section 3.3). We discuss mass transport limitations on Rh and Pt in Section 3.4, where we analyze the rate of O_2 conversion at the catalyst entrance. To illustrate how information on mass transport can be extracted from spatial profiles, we calculate an average O_2 mass transport coefficient and compare it with literature values. Finally, we compare exit species flow rates and temperatures with thermodynamic calculations to show how close the reaction is brought to thermodynamic equilibrium on the Rh and Pt foam catalyst (Section 3.5).

2. Materials and methods

2.1. *Catalyst preparation*

The foam catalysts used in this work were prepared by impregnating α-Al_2O_3 foam supports (≈10 mm long, 16.5 mm diameter, 80 pores per linear inch, Vesuvius High-Tech) with aqueous $Rh(NO_3)_3$ and H_2PtCl_6 precursor solutions. As verified by scanning electron microscopy on used catalysts (not shown), the different precursors did not lead to significantly different particle sizes or morphologies. At the high temperatures prevailing in an autothermal foam (>1000 °C), both metals sintered, forming several hundred nm large crystals exposing low index surfaces typical for their fcc lattice. Previously reported spatially resolved X-ray absorption spectroscopy results [21,22] indicate that Rh and Pt are in an oxidized state at the catalyst entrance and in a reduced metallic state as soon as H_2 is formed in the catalyst bed. However, these studies were performed in very diluted 6% CH_4/3% O_2/He mixtures and at a maximum temperature of 500 °C. Under our reaction conditions ($T > 1000\,°C$), H_2 is formed from the beginning of the catalyst on and both metals are probably in a reduced metallic state over the entire catalyst length.

The channels for the capillary sampling (diameter = 0.7 mm) were drilled before impregnation. A washcoat was not applied. The concentration of the precursor solution was such that each foam catalyst was loaded with 5% Rh or Pt by weight. Earlier studies by Degenstein et al. [23] showed that conversion and selectivity values in an autothermal CPO reaction were rather insensitive to noble metal loading in a range of 0.05 to 10 wt%. A loading of 5 wt% is in the middle of this range. The impregnation was performed in multiple steps with drying in vacuum at room temperature between steps. The Rh catalysts were calcined for 6 h at 600 °C in a furnace in air, and the Pt catalysts were calcined for 5 h at 500 °C in a flowing H_2/N_2 mixture (10 vol% H_2) to avoid Pt losses by formation of volatile platinum oxides. The noble metal load of the final catalysts was verified to be 5 ± 1 wt% from the weight increase with respect to the uncoated foam.

2.2. *Reactor and capillary sampling system*

The reactor and capillary sampling system used in this study is a further development of the setup that we used to measure the first species and temperature profiles for the methane CPO in adiabatic foams reported in the literature [17,18]. A schematic of the setup is shown in Fig. 1.

As in the earlier reactor, the catalyst foam is sandwiched between front and back heat shields (empty foams), wrapped tightly in alumo-silicate paper and placed in a quartz reaction tube (i.d. = 19 mm, length = 7 cm). The sampling capillary (o.d. = 0.65 mm, quartz) contains a side sampling orifice (diameter 200–300 µm) and a thermocouple (type K, Omega) aligned with the sampling orifice (see inset of Fig. 1). The quartz sampling capillary and thermocouple meet in a stainless steel tee (1/16″, 0.029″ bore, Valco), the third port of which is connected to a stainless steel capillary (1/16″, 0.010″ bore) that discharges into the inlet valve of the mass spectrometer. A pump generates a vacuum at the end of the stainless steel capillary (∼100 Pa), forcing the gases from the sampling orifice into the mass spectrometer. The sampling flow rate is determined largely by the choked flow in the stainless steel capillary and is on the order of 10 ml min^{-1}, which is a negligible disturbance of the flow considering a total flow rate of 4.7 slpm. Moving the capillary/thermocouple assembly up and down allows measuring species and temperature profiles along the centerline of the catalyst. The measured temperature is a gas temperature as the thermocouple is in thermal contact with the flowing gas but not with the catalyst surface.

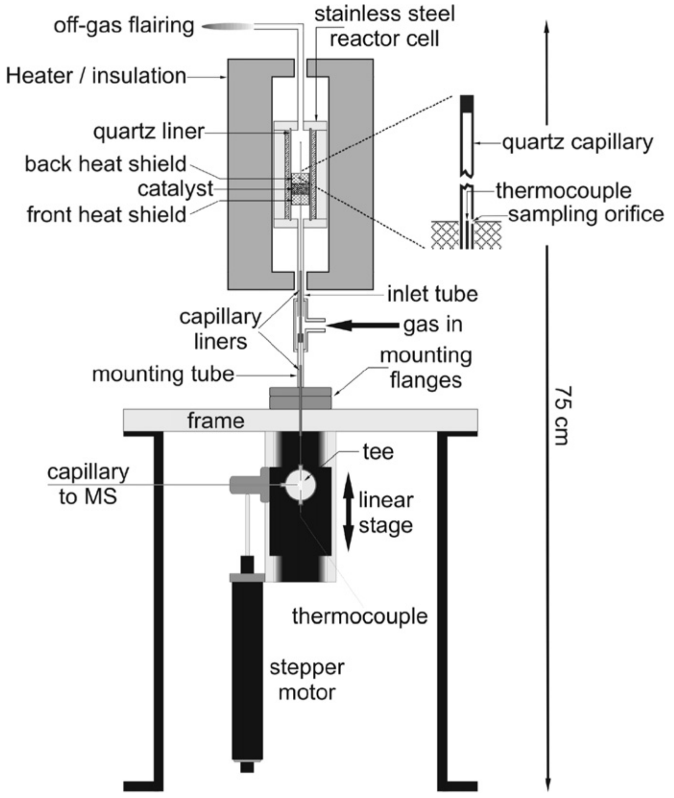

Fig. 1. Reactor setup and capillary sampling system.

A quartz liner is used in the reactor, because stainless steel might become catalytically active at temperatures above 1000 °C, which prevail in the reaction zone. Even though stainless steel has a low heat conductivity, the quartz liner is surrounded by alumo-silicate paper to reduce radial heat losses. The stainless steel reaction cell is placed into a ceramic heater (Omega). For reaction light-off, the heater is switched on; after light-off, the heater is switched off and serves as an additional insulation around the stainless steel cell. The five layers of insulation (alumo-silicate paper, quartz liner, alumo-silicate paper, stainless steel cell, ceramic heater) minimize heat losses, so that the reactor can be considered adiabatic.

The reaction cell is self-supported on a steel mounting frame with stainless steel inlet and outlet tubes. The sampling capillary is guided in steel capillary liners to avoid any bending leading to uncertainties in the sampling orifice position. The compact and rigid self-supported construction of the reactor provides precise geometric alignment and is easy to dismantle and reassemble.

Another important improvement is the automated capillary movement by a stepper motor (T-LA60, Zaber Technologies) mounted underneath the reactor. Whereas the first profiles [17,18] were measured by manually turning a micrometer (∼50 data points in 1 h), each profile in this work consists of about 1500 data points measured in 10 min. The automatization allowed larger experimental campaigns to be conducted than in the initial studies.

In this work we present spatial profiles on Rh and Pt catalysts at 15 different inlet stoichiometries ranging from C/O = 0.6 to 2.6. The composition of each mixture was calculated according to (i) the C/O ratio (ratio of carbon to oxygen atoms in the feed, $C/O = F_{CH_4}/(2F_{O_2})$), (ii) a constant inlet flow rate of $F_{tot} = 0.208$ mol/min (≈4.7 slpm), and (iii) an Ar/O_2 ratio of 79/21.

2.3. *Mass spectrometry and data analysis*

The mass spectrometer used for this study was a quadrupole instrument (UTI model 100C) with an electron impact ionizer (ionization energy 70 eV) and an electron multiplier as detector. The mass spectrometer was calibrated for H_2 $m/z = 2$ amu, CH_4 $m/z = 15$ amu, CO $m/z = 28$ amu, O_2 $m/z = 32$ amu, and CO_2 $m/z = 44$ amu using Ar $m/z = 40$ amu as an internal standard. In all measurements, the Ar/O_2 ratio was 79/21, the N_2/O_2 ratio in air that might be the oxidant in a technical process.

After substraction of the baseline, the peak areas for the species of interest were calculated by numerical integration using the trapezoidal rule. The Ar-normalized signals were converted into molar flow rates using the sensitivity factors from the calibration. Besides the contribution from CO_2 to the CO signal at 28 amu, cross-sensitivities were negligible. Because H_2O adsorption could not be totally avoided, the H_2O profiles were calculated from the H and O atom balances using least squares optimization. The atom balances ΔH, ΔC, and ΔO for all positions were between the following limits: $2\% < \Delta H < 5\%$, $-1\% < \Delta C < 3\%$, $-13\% < \Delta O < 5\%$.

In contrast to the profiles given by [17,18], where each data point is an average of about 150 full spectra, here the continuous capillary movement results in a single data point at each position. To remove the high-frequency noise caused by the mass spectrometer, each raw profile was slightly smoothed by a 15-point FFT filter (Origin, OriginLab). The smoothing does not affect the continuously varying profiles themselves, because their low frequencies are very different from the high frequencies of the noise.

3. Results and discussion

3.1. *Temperature, conversion, and selectivity at reactor exit*

What has been available so far in the literature for the methane CPO were reactor exit data showing CH_4 and O_2 conversions; selectivities to H_2, CO, H_2O, and CO_2; and exit temperatures. Fig. 2 shows these data for all C/O ratios studied in this work.

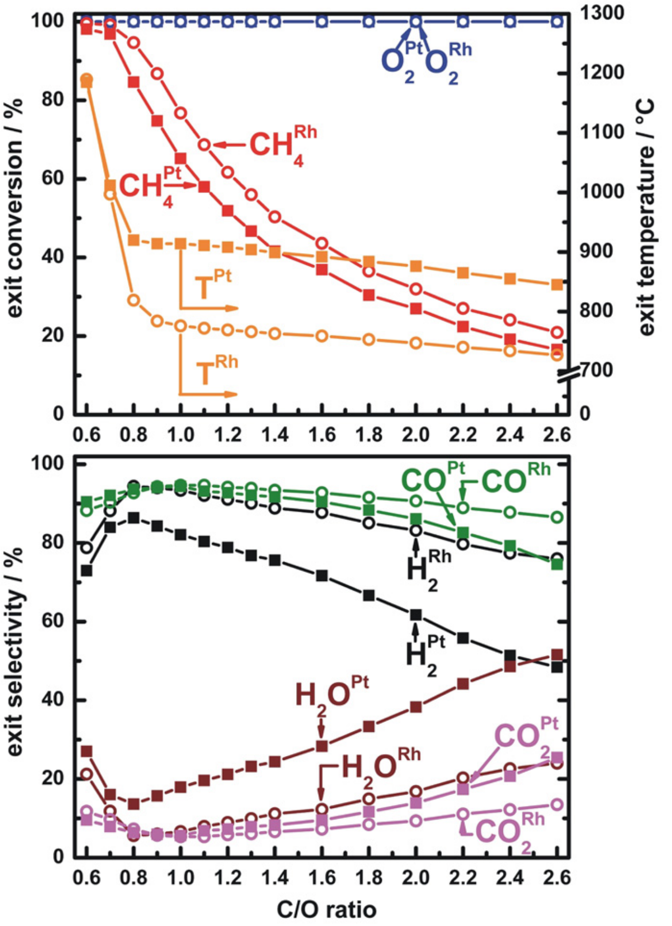

Fig. 2. Temperature, conversion and selectivity at reactor exit using a 10 mm long, 80 ppi α-Al_2O_3 foam catalyst coated with 5 wt% Rh (○) and 5 wt% Pt (■) for C/O = 0.6–2.6. Total inlet flow 4.7 slpm, atmospheric pressure.

O_2 conversion is 100% on both metals regardless of whether a methane-rich mixture (C/O = 2.6) or a methane-lean mixture (C/O = 0.6) is fed to the reactor. For C/O = 0.6 and 0.7 on Rh, CH_4 conversion was higher than 99% and only slightly lower on Pt (98 and 97%, respectively). At higher C/O, the CH_4 conversion dropped rapidly, because O_2 is the stoichiometrically-limiting component. For the same C/O, the exit CH_4 conversion was always higher on Rh than on Pt.

The lower H_2 and CO selectivities on Pt and the higher exit temperatures on Pt clearly show that Pt favored the strongly exothermic total oxidation of CH_4 to CO_2 and H_2O, whereas Rh was the better partial oxidation catalyst, favoring the less endothermic H_2 and CO formation. However, there is no way to tell from the reactor exit data how these different conversion, selectivity, and temperature values are achieved inside the catalyst. It could be that Reaction (2) is the main reaction pathway on both metals, just with different values of x and y on Pt and Rh. It also could be true that the reaction pathway on both metals is a combination of the Reactions (3), (4), and (5) with different rates R_3, R_4, and R_5 on Pt and Rh, or that the chemical transformations occur by some other pathway. In addition,

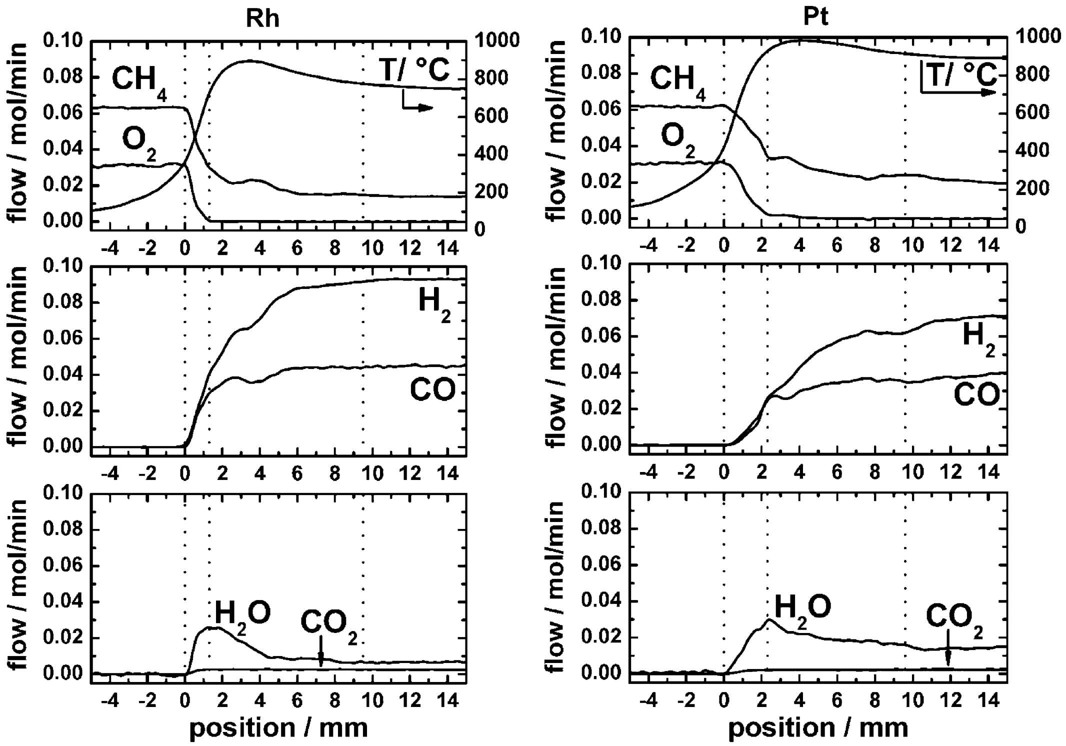

Fig. 3. Spatially resolved species and temperature profiles for syngas stoichiometry (C/O = 1.0) and a total inlet flow of 4.7 slpm. Rh (left panels), Pt (right panels). 'Oxidation zone' between first and second dotted line. 'Steam-reforming zone' between second and third dotted line.

the observation that the selectivity difference between Rh and Pt is more pronounced for the competing products H_2/H_2O than for the competing products CO/CO_2 cannot be explained from reactor exit data only. High resolution spatial profiles inside the catalyst can answer these questions, as discussed in the following Sections 3.2 and 3.3.

3.2. *Profiles at syngas stoichiometry*

A comparison of the species and temperature profiles on Rh and Pt for syngas stoichiometry (C/O = 1.0, Eq. (1)) and 4.7 slpm flow rate is displayed in Fig. 3. Qualitatively, the profiles look similar on both metals; however, there are pronounced quantitative differences. In what follows, we ignore the small plateaus, bumps, and dips shown in the profiles in Fig. 3, because these are usually irreproducible features caused by blocked pores or cavities along the sampling line.

Table 1
Comparison of Rh and Pt profiles at C/O = 1.0 and 4.7 slpm inlet flow rate: z = axial coordinate, end oz = end oxidation zone (end oz Rh at $z = 1.3$ mm, end oz Pt at $z = 2.3$ mm), exit = exit catalyst (exit Rh at $z = 9.5$ mm, exit Pt at $z = 9.6$ mm), T^{gas} = gas temperature, F = species molar flow rates, equil. = values at equilibrium (see Fig. 10)

	Rh	Pt	Rh end oz	Pt end oz	Rh exit	Pt exit	Equil.
z ($T^{\text{gas}}_{\text{max}}$) (mm)	3.5	4.1	–	–	–	–	–
$T^{\text{gas}}_{\text{max}}$ (°C)	895	983	–	–	–	–	–
T^{gas} (°C)	–	–	728	928	776	914	690
F_{CH_4} (mol min^{-1})	–	–	0.030	0.034	0.015	0.024	0.010
F_{O_2} (mol min^{-1})	–	–	0.000	0.002	0.000	0.000	0.000
F_{H_2} (mol min^{-1})	–	–	0.041	0.026	0.092	0.062	0.097
F_{CO} (mol min^{-1})	–	–	0.030	0.025	0.044	0.035	0.046
F_{H_2O} (mol min^{-1})	–	–	0.026	0.029	0.007	0.016	0.006
F_{CO_2} (mol min^{-1})	–	–	0.002	0.003	0.003	0.003	0.005

3.2.1. *Oxidation zone*

The reactant profiles (upper panels) show a zone at the catalyst entrance in which O_2 and CH_4 are rapidly consumed until O_2 is fully converted. This zone, called the "oxidation zone" hereinafter, and is located between the first and the second dotted line in Fig. 3. Measurements on different foams revealed that the absolute length of the oxidation zone differs slightly from foam to foam, but the oxidation zone is generally longer on Pt than on Rh (here 2.3 vs 1.3 mm, respectively).

About 52 and 45% CH_4 is converted in the oxidation zone on Rh and Pt, respectively; that is, CH_4 conversion is higher on Rh than on Pt. The predominant oxidation products on both metals are H_2, CO, and H_2O. CO_2 is formed only in small amounts in the oxidation zone. Table 1 summarizes temperatures and molar flow rates of reactants and products at the end of the oxidation zone (columns 3 and 4) and at the end of the catalyst (columns 5 and 6). The equilibrium flow rates for adiabatic conditions (p, H = const.) are displayed for comparison (column 7).

The amounts of H_2 and CO formed in the oxidation zone are higher on Rh than on Pt (H_2: 0.041 vs 0.026 mol min^{-1}; CO: 0.030 vs 0.025 mol min^{-1}, respectively). Pt forms more total oxidation products in the oxidation zone than Rh (H_2O: 0.029 vs 0.026 mol min^{-1}, CO_2: 0.003 vs 0.002 mol min^{-1}, respectively). Based on these flow rates, the selectivities to H_2 and CO can be calculated and from that the values of x and y (see Eq. (2)) to summarize the chemistry in the oxidation zone on Rh and Pt for syngas stoichiometry (C/O = 1.0):

$$S_{H_2} = \frac{F_{H_2}}{F_{H_2} + F_{H_2O}} = \frac{x}{2} \quad \Rightarrow \quad S_{H_2}^{Rh} = 0.6, \quad S_{H_2}^{Pt} = 0.5,$$

$$\Rightarrow \quad x^{Rh} = 1.2, \quad x^{Pt} = 1.0, \tag{6}$$

$$S_{CO} = \frac{F_{CO}}{F_{CO} + F_{CO_2}} = y \quad \Rightarrow \quad S_{CO}^{Rh} = 0.9, \quad S_{CO}^{Pt} = 0.9,$$

$$\Rightarrow \quad y^{Rh} = 0.9, \quad y^{Pt} = 0.9, \tag{7}$$

$$\text{Rh: } CH_4 + 0.95O_2 \rightarrow 1.2H_2 + 0.9CO + 0.8H_2O + 0.1CO_2, \quad \Delta H^\circ_{r,\mathrm{Rh}} = -257\ \mathrm{kJ\,mol^{-1}}, \tag{8}$$

$$\text{Pt: } CH_4 + 1.05O_2 \rightarrow 1.0H_2 + 0.9CO + 1.0H_2O + 0.1CO_2, \quad \Delta H^\circ_{r,\mathrm{Pt}} = -306\ \mathrm{kJ\,mol^{-1}}. \tag{9}$$

Equations (6)–(9) show that Rh forms H_2 more selectively than Pt in the presence of gas phase O_2, whereas the selectivities to CO are about the same on both metals for C/O = 1.0. But because the CH_4 conversion is higher on Rh than on Pt, the yields of both H_2 and CO are higher in the oxidation zone on Rh than on Pt. In Section 3.3.2, we show that Rh forms also CO more selectively than Pt, but this difference becomes important only if C/O > 1.0.

3.2.2. *Steam-reforming zone*

The point of total conversion of gas phase O_2 is clearly reflected in the profiles of all other species. Methane conversion continues on both metals, but the conversion rate slows significantly. The H_2 and CO formation rates (profile slopes) drop, that of CO more than that of H_2. The CO_2 formation stops at this point. H_2O now becomes the co-reactant to CH_4; therefore, the H_2O flow rate goes through a maximum at the end of the oxidation zone. Because CH_4 and H_2O react in this second zone with each other (Eq. (4)), it is designated the "steam-reforming zone," located between the second and third dotted lines in Fig. 3. The developing profiles in the steam-reforming zone clearly reflect the H_2/CO molar ratio of 3/1 predicted by Eq. (4). The CO_2 molar flow rate remains constant after gas phase O_2 has been fully consumed. CO_2 reforming (Eq. (5)) is not observed.

H_2 and CO are the only products formed in the steam-reforming zone. The yields of H_2 and CO obtained in the steam-reforming zone are determined by the CH_4 conversion. As in the oxidation zone, Rh converts more CH_4 than Pt in the steam-reforming zone. At C/O = 1.0, 24% of the CH_4 fed to the reactor is converted in the steam-reforming zone on Rh compared with 16% on Pt.

3.2.3. *Temperature profiles and heat transport limitations*

The temperature profiles shown in Fig. 3 reflect the heat production by the strongly exothermic oxidation reactions in the oxidation zone followed by heat consumption due to the strongly endothermic steam reforming. The Pt catalyst operates at higher temperatures than the Rh catalyst because more heat is generated in the oxidation zone ($\Delta H_{r,\mathrm{Pt}} = -306\ \mathrm{kJ\,mol^{-1}}$ vs $\Delta H_{r,\mathrm{Rh}} = -257\ \mathrm{kJ\,mol^{-1}}$, respectively) and less heat is consumed, because endothermic steam reforming is slower on Pt than on Rh.

As shown in Table 1, the oxidation zone on Rh has a length of 1.3 mm and that on Pt has a length of 2.3 mm, but the maximum gas temperature is measured at 3.5 and 4.1 mm, respectively. Heat transport limitations are the reasons why the maximum gas temperature is measured about 2 mm behind the oxidation zone on both catalysts and that the temperature rise inside the oxidation zone is about the same on both catalysts ($\sim 330\ \mathrm{K\,mm^{-1}}$ at C/O = 1.0).

The thermocouple inside the capillary has thermal contact with the gases but not with the catalyst surface; therefore, all thermocouple temperature profiles in this work are gas temperatures. Recent pyrometric measurements by us (not shown here) and others [24] and also numerical simulations [4,9,17, 24–26] show that severe heat transport limitations occur along the catalyst axis. In the oxidation zone, the surface temperature is much higher than the gas temperature as the heat generation at the catalyst surface is much faster than the heat transport to the incoming cold gases. Exactly the opposite holds for the steam-reforming zone. Here, endothermic surface steam-reforming cools the catalyst faster than heat is transferred from the now hot gases to the solid structure. At the catalyst exit, gas and surface temperature are roughly equilibrated.

3.2.4. *Mechanism of the methane CPO at syngas stoichiometry*

From the high-resolution spatial profiles, it can be concluded that the mechanism of the methane CPO is a combination of partial oxidation (Eq. (2)) and steam reforming (Eq. (4)). The overall yields of H_2 and CO are higher on Rh than on Pt for three reasons:

(1) Rh activates CH_4 more efficiently in the presence of O_2 than Pt.
(2) Rh forms H_2 more selectively in the presence of O_2 than Pt. CO selectivities are comparable at C/O = 1.0.
(3) Rh is the more active steam-reforming catalyst.

Especially their different ability to catalyze steam reforming makes Rh the better catalyst for the methane CPO. After only 5 mm on Rh, the H_2O flow rate has nearly reached its equilibrium value, and H_2 and CO production level off. On Pt, steam reforming is significantly slower, and the rate of H_2O conversion is nearly constant across the steam-reforming zone. H_2 and CO production continue on the Pt catalyst until the end, and a catalyst longer than 10 mm is required to bring the reaction comparably close to equilibrium as within 5 mm on Rh (see Table 1 and Section 3.5). The reason for the postcatalytic syngas production on the Pt catalyst is the presence of Pt deposits in the back heat shield transported there from the hot oxidation zone in the form of volatile platinum oxides (e.g., PtO_2).

3.3. Mechanism of the methane CPO at other C/O ratios

The discussion of the mechanism of the methane CPO in Section 3.2 was focused on syngas stoichiometry (C/O = 1.0). We showed that H_2 and CO formation occur by partial oxidation at the first 1–3 mm of the catalyst, followed by steam-reforming downstream with no contribution from CO_2 reforming.

In this section we extend the discussion to other reactant stoichiometries and show that the reaction mechanism always remains a sequence of partial oxidation and steam reforming but with changing relative contributions to the final yields of H_2 and CO. The data show that the contribution of partial oxidation depends on the catalyst temperature, which in turn is a function of C/O. Partial oxidation provides high yields of H_2 and CO at high catalyst temperatures (i.e., at low C/O). Optimal values are reached around C/O = 0.8. At low catalyst temperature (high C/O), nearly no H_2 and only small amounts of CO are formed by partial oxidation. The low-temperature mechanism for syngas formation is total oxidation of CH_4 to H_2O and CO_2, followed by steam reforming.

We begin our discussion in Section 3.3.1 by presenting spatial profiles measured for a wide range of reactant stoichiometries. In Section 3.3.2, we compare Rh and Pt with respect to selectivity and yield of H_2 and CO formation in the oxidation zone. In Section 3.3.3, we compare the contributions of partial oxidation and steam reforming to the overall production of H_2 and CO on each metal and show their dependence on C/O and catalyst temperature.

3.3.1. Spatial profiles for C/O = 0.6–2.6

Fig. 4 shows how the profiles for selected species (O_2, H_2, and CO) and the gas temperature develop from C/O = 0.6–2.6 (only ΔC/O = 0.2 displayed). Qualitatively, the profiles develop similarly at each C/O ratio. All profiles show H_2 and CO production by partial oxidation followed by steam reforming. The H_2 and CO flow rates increase with decreasing C/O, reach a maximum at C/O = 0.8, and decrease sharply thereafter. The gas temperature increases slowly up to C/O = 1.0 and faster at lower values, because of enhanced H_2O formation. At C/O = 0.6, the gas temperatures approach or even exceed 1200 °C, which corresponds to catalyst surface temperatures approaching 1400 °C. As can be seen from the increased length of the oxidation zone, the catalyst becomes irreversibly deactivated at these temperatures, probably by sintering of the metal particles or metal losses from volatile oxides. Therefore, hereinafter we omit C/O = 0.6 from the discussion.

3.3.2. Product selectivities in the oxidation zone

Fig. 5 compares Rh and Pt with respect to CH_4 conversion (X) and product selectivities (S) at the end of the oxidation zone ($X_{O_2} = 100\%$). It also displays the adiabatic temperatures $T^{\text{ad.}}_{\text{calc.}}$ calculated for the gas composition at the end of the oxidation zone. These temperature values are upper limits for the catalyst surface temperature at this position.

Because O_2 is the stoichiometrically limiting reactant, CH_4 conversion decreases with increasing C/O. For all C/O, CH_4 conversion is higher on Rh than on Pt. Rh consumes more CH_4 with the same amount of O_2, because it forms more partial oxidation products (H_2 and CO) than Pt, which produces more H_2O and CO_2. But because total oxidation releases more heat than partial oxidation, the Pt catalyst operates at a higher temperature than the Rh catalyst ($T^{\text{ad.,Pt}}_{\text{calc.}} > T^{\text{ad.,Rh}}_{\text{calc.}}$), especially at C/O < 1.4, where CH_4 conversion is high.

The lower panel of Fig. 5 displays the selectivities to H_2, CO, H_2O, and CO_2 at the end of the oxidation zone of the Rh and the Pt catalyst. For each metal, selectivities to H_2 and CO are highest on a hot catalyst (C/O $\leqslant$ 1.0) and decrease if the catalyst operates at colder temperatures (increasing C/O). This trend is opposite to most other partial oxidation reactions, in which the partial oxidation products are formed in kinetic control and higher temperatures lead to more total oxidation (H_2O and CO_2 formation). However, in the methane CPO, H_2 and CO are thermodynamically favored at high temperatures [3], and the observed selectivities reflect this thermodynamic trend. For example, at C/O = 0.7, where the adiabatic temperature is about 1260 °C on Rh and about 1350 °C on Pt, the H_2 selectivities are 60 and 50%, respectively. At C/O = 2.6, the adiabatic temperature at the end of the oxidation zone is about 800 °C on both metals, and the H_2 selectivities are only 33% on Rh and 17% on Pt. A similar trend holds for CO. For C/O = 0.7, the CO selectivity is about 90% on both metals and drops to 81% on Rh and 65% on Pt if the C/O is decreased to 2.6.

Comparing Rh and Pt shows that Rh displays higher selectivities to H_2 and CO. This difference increases with decreasing catalyst temperature (C/O). At C/O = 0.7, Rh has a 10% higher selectivity to H_2 than Pt, but their CO selectivities are about the same. At C/O = 2.6, Rh has a 16% higher selectivity to H_2 and a 16% higher selectivity to CO. The higher H_2 selectivity on Rh can be attributed to a higher activation barrier for the formation of OH ($H_s + O_s \rightarrow OH_s$), which leads to H_2O. The barrier for OH formation is 84 kJ mol^{-1} on Rh but only 10 kJ mol^{-1} on Pt [1]. The higher CO selectivity on Rh is probably caused by the lower energy barrier for CO_2 redissociation. According to [1], a quasi-equilibrium is established for $CO_s + O_s \rightleftarrows CO_{2,s}$ on the Rh and Pt surfaces. Whereas the forward reaction barrier is similar for both metals (Rh: 105 kJ mol^{-1}, Pt: 100 kJ mol^{-1}), the redissociation of CO_2 is much stronger activated on Pt than on Rh (Rh: 176 vs 134 kJ mol^{-1}).

Another factor favoring the formation of partial oxidation products is the presence of strong O_2 mass transport limitations on Rh but not on Pt. We discuss this in more detail in Section 3.4.

3.3.3. Contribution of partial oxidation and steam reforming to syngas formation

In the preceding section we showed how the oxidation zone selectivity depends on the catalyst and the C/O ratio (catalyst temperature). In this section, we quantify the contribution of partial oxidation and steam reforming to the final syngas yield for C/O = 0.7–2.6. The corresponding data are summarized in Fig. 6.

The CH_4 conversion at the catalyst exit is a sum of the CH_4 conversion by partial oxidation and CH_4 conversion by steam

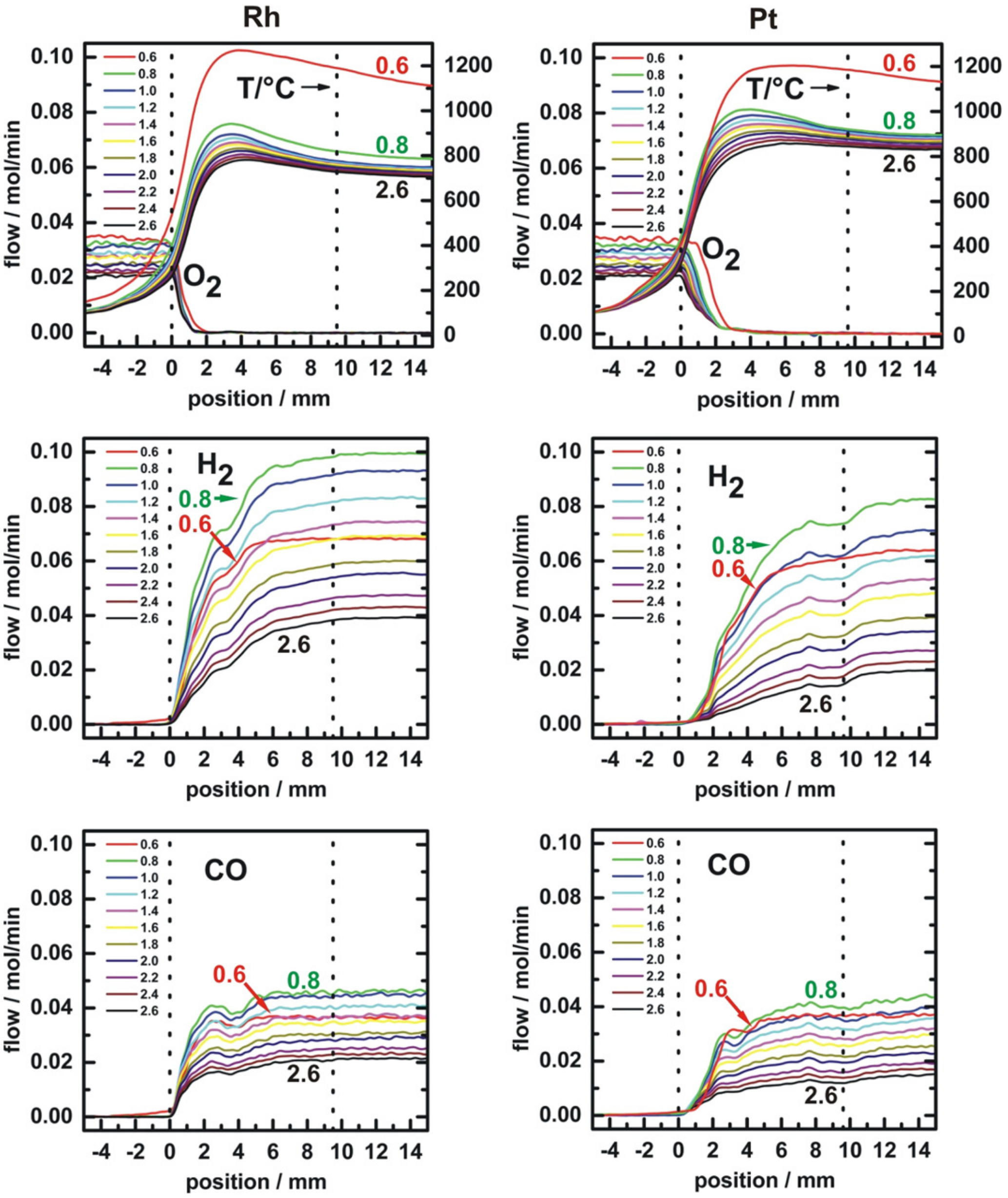

Fig. 4. Gas temperature, oxygen, hydrogen and carbon monoxide profiles for C/O ratios from 2.6 to 0.6. Total inlet flow 4.7 slpm. Rh (left panels), Pt (right panels). Catalyst section between dotted lines.

reforming. As shown in the upper panels, the difference between the CH_4 conversion at the catalyst exit and the end of the oxidation zone decreases with increasing C/O. This reflects the decreasing rate of the highly endothermic steam reforming ($\Delta H_r^\circ = +206\ \text{kJ mol}^{-1}$) with the decreasing catalyst temperature. At C/O = 0.7 steam reforming increases the CH_4 conversion on Rh from 69% at the end of the oxidation zone to ≈100% at the catalyst exit. Similar values are found on Pt. At C/O = 2.6, the catalyst operates much colder, and steam reforming increases the CH_4 conversion on Rh by only 6%, from 15% at the end of the oxidation zone to 21% at the catalyst exit (Pt similar).

Separating the H_2 and CO selectivities into the contributions from partial oxidation and steam reforming shows that steam reforming significantly increases exit H_2 selectivity but has only a small effect on exit CO selectivity. This is because the H_2 selectivity is determined by $S_{H_2} = F_{H_2}/(F_{H_2} + F_{H_2O})$ whereas the selectivity to CO is determined by $S_{CO} = F_{CO}/(F_{CO} + F_{CO_2})$; F being molar flow rates. Steam-reforming consumes H_2O and produces 3 mol H_2 per 1 mol H_2O, but produces only 1 mol CO per 1 mol H_2O at a constant CO_2 flow rate in the steam-reforming zone.

The conversion values (X) and selectivity values (S) can be multiplied to give H_2 and CO yields ($Y = XS$) that are proportional to our experimentally observed molar flow rates. By calculating the ratio between the yield at the end of the oxidation zone and the yield at the exit of the catalyst ($Y(H_2^{\text{end oz}})/Y(H_2^{\text{exit}})$ and $Y(CO^{\text{end oz}})/Y(CO^{\text{exit}})$, respectively), the contribution of partial oxidation to the overall H_2 and CO production can be quantified. The results are very inter-

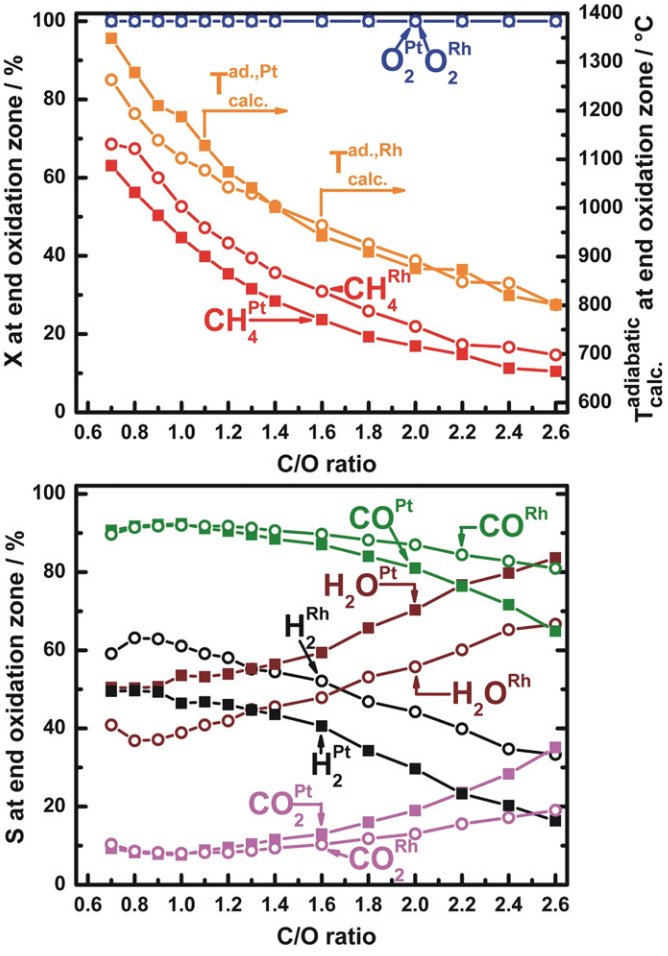

Fig. 5. CH_4, O_2 conversion (X); calculated adiabatic temperature (T^{ad}_{calc}) and H_2, CO, H_2O, CO_2 selectivities (S) at the end of the oxidation zone for C/O = 0.7–2.6. Rh (○) provides higher H_2 and CO selectivities than Pt (■). On both metals, H_2 and CO selectivity is highest between $0.8 \leqslant C/O \leqslant 1.0$ (high catalyst temperature) and decreases with increasing C/O (decreasing catalyst temperature).

esting, demonstrating that the contribution of partial oxidation to the exit H_2 and CO yield varies widely depending on the C/O ratio, that is, the catalyst temperature. On the "hot" Rh catalyst (e.g., C/O = 0.8), partial oxidation can contribute as much as 61%/87% = 70% to the exit CO yield and as much as 42%/89% = 47% to the exit H_2 yield. The other extreme is a "cold" Pt catalyst (e.g., C/O = 2.6), for which partial oxidation contributes 6.5%/12.5% = 52% to the exit CO yield but only 1.7%/8.0% = 21% to the exit H_2 yield. 79% of all H_2 formed over the Pt catalyst at C/O = 2.6 is produced by steam reforming.

These numerical values illustrate that the sequence in which the products of the methane CPO are observed is a strong function of the reaction conditions. The catalyst temperature can be identified as one important parameter that determines the amounts of H_2 and CO formed by partial oxidation and the amounts formed by steam reforming. In the next section we analyze the O_2 spatial profiles to see whether mass transport limitations lead to a lower O_2 concentration at the catalyst surface than in the bulk gas phase, which would have an additional impact on the H_2 and CO selectivities.

3.4. Mass transport limitations on Rh and Pt

Mass transport limitations are a common phenomenon in short-contact time catalysis and require attention to proper catalyst bed design. Numerical simulations indicate that the methane CPO is O_2 mass transport-limited on both Rh [24,27] and Pt [4]. With the spatial profiles over a wide range of stoichiometries ratios at hand, these predictions now can be verified.

3.4.1. Oxidation zone on Rh and Pt

In Fig. 4, it is striking that except for C/O = 0.6, where very high temperatures deactivate the catalyst irreversibly, the length of the oxidation zone is independent of the C/O ratio. To explain this observation, Fig. 7 shows the O_2 profiles on Rh and Pt expanded with two selected positions marked. Position one is the point at which the O_2 molar flow rate has dropped to 50% of its inlet value, and position two is the end of the oxidation zone, where the O_2 flow rate approaches zero. On Rh, the axial position where 50% O_2 conversion is reached remains the same to a good approximation, independent of the initial O_2 concentration in the feed. This invariance points to a first-order dependence in O_2, which, in agreement with the literature, we attribute to an O_2 mass transport limitation [24,27]. We give the mathematical argument for this interpretation in Section 3.4.2. The same invariance would be observed in kinetic control if the methane CPO was first-order in O_2. We do not believe that this is the case, however, because kinetic studies on Rh [9] report a zeroth-order O_2 dependence. On Pt, the axial position at which 50% O_2 conversion is reached increases linearly with the inlet O_2 concentration. If a line is fitted through the points and extrapolated to an inlet O_2 concentration of zero, then the line goes through the origin. We show in Section 3.4.3 that this result indicates a constant reaction rate in the oxidation zone on Pt, that is, kinetic control. Toward the end of the oxidation zone on Rh and Pt, the gas-phase O_2 concentration becomes very small and mass transport rate-limiting, and thus all O_2 profiles end at the same point. We next provide the mathematical arguments for this interpretation.

3.4.2. Mass transport control on Rh

The length of the oxidation zone depends on the interplay of how quickly O_2 is converted at the catalyst surface and how quickly it can be transported to the catalyst surface from the bulk gas phase. In the random porous network of a foam catalyst, the bulk gas phase is well mixed, and high axial velocities render axial species diffusion negligible compared with convection. However, radial diffusion cannot be neglected. Therefore, the rate of O_2 conversion at the catalyst entrance can be described by a one-dimensional model with mass transport resistance at the catalyst surface (Eq. (10)):

$$\rho u \frac{dY^b_{O_2}}{dz} = \frac{S}{V} \cdot k^m_{O_2} \cdot \rho \cdot \left(Y^s_{O_2} - Y^b_{O_2}\right). \qquad (10)$$

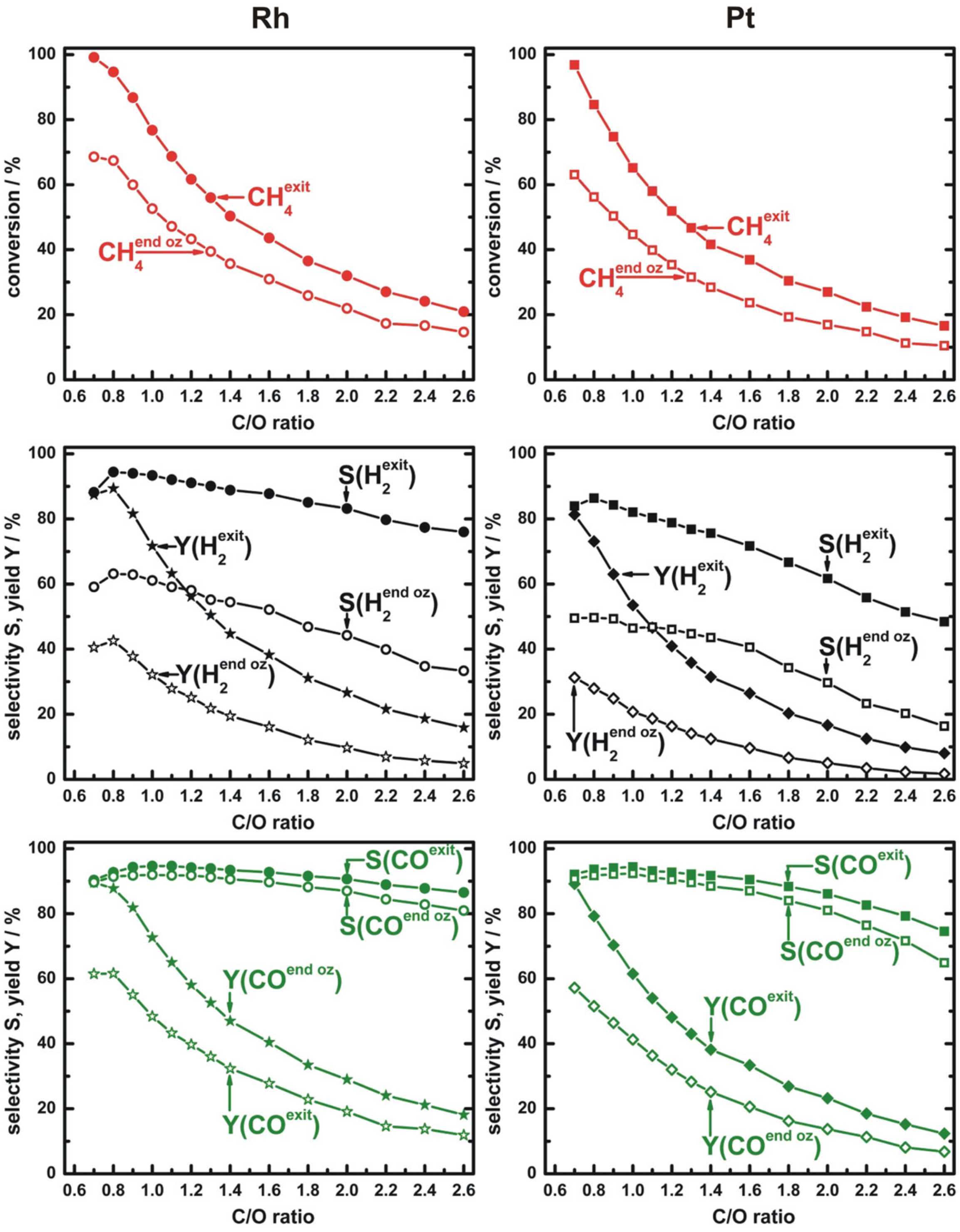

Fig. 6. CH_4 conversion; H_2, CO selectivities and H_2, CO yields on Rh (left panels) and Pt (right panels) for C/O = 0.7–2.6. Comparison of values at the end of the oxidation zone (open symbols) with values at the catalyst exit (full symbols).

In Eq. (10), ρ is the gas density in $\mathrm{kg/m^3}$, u is the gas velocity in m/s, $Y_{O_2}^{b}$ and $Y_{O_2}^{s}$ are the O_2 mass fractions in the bulk gas phase and close to the surface, respectively, z is the axial coordinate in m, S/V is the ratio of the catalytic active surface to the pore volume in $\mathrm{m^{-1}}$, and $k_{O_2}^{m}$ is the O_2 mass transport coefficient in m/s. Even though calculation of the oxidation zone lengths is beyond the scope of this work and has been addressed previously [17], Eq. (10) simplifies in case of full mass transport control ($Y_{O_2}^{s} = 0$), to the following:

$$-\frac{\mathrm{d}Y_{O_2}^{b}}{Y_{O_2}^{b}} = \frac{S}{V} \cdot \frac{k_{O_2}^{m}}{u}\,\mathrm{d}z. \tag{11}$$

The O_2 mass fraction drops along the axial coordinate and at a given position, z, is only a fraction, $f = Y_{O_2}^{bz}/Y_{O_2}^{b\mathrm{in}}$, of its inlet

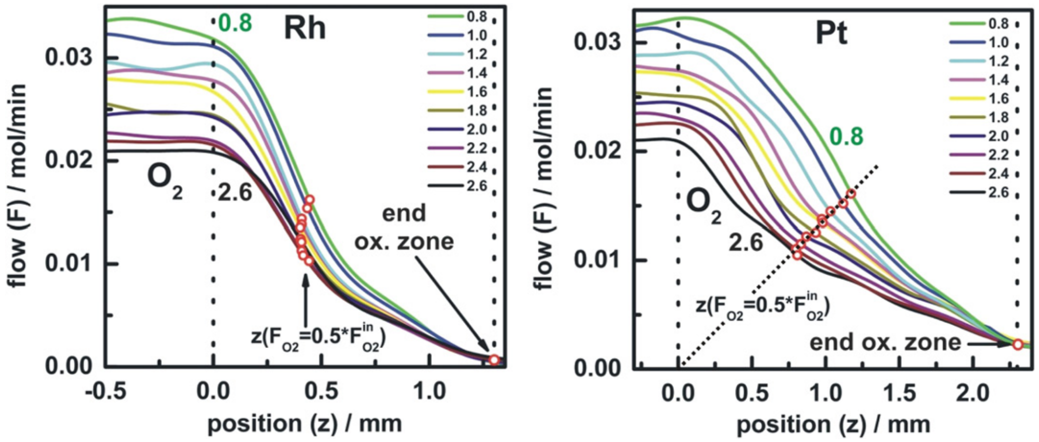

Fig. 7. Expanded O_2 profiles in the oxidation zone on Rh (left panels) and on Pt (right panels) for C/O ratios from 0.8 to 2.6. The distance for 50% O_2 conversion is nearly constant for Rh but varies linearly for Pt indicating full mass transport control on Rh (Eq. (12)) but zeroth-order kinetic control on Pt (Eq. (14)).

value. Integration from the catalyst entrance to this point in the oxidation zone gives Eq. (12). Because both the oxygen mass transport coefficient $k_{O_2}^m$ and the gas velocity u are T, and hence z-dependent, we introduce an average oxygen mass transport coefficient, $\overline{k_{O_2}^m}$, and an average gas velocity, $\bar{u}$, to make these terms independent of z over the length scale investigated:

$$-\int_{Y_{O_2}^{bin}}^{f\cdot Y_{O_2}^{bin}} \frac{\mathrm{d}Y_{O_2}^b}{Y_{O_2}^b} = \frac{S}{V}\cdot\frac{\overline{k_{O_2}^m}}{\bar{u}}\int_0^z \mathrm{d}z \Rightarrow z = \ln\left(\frac{1}{f}\right)\cdot\frac{V}{S}\cdot\frac{\bar{u}}{\overline{k_{O_2}^m}}. \qquad (12)$$

The integrated form of Eq. (12) demonstrates a simple relationship between the mean O_2 mass transport coefficient and the position at which the O_2 mass fraction has dropped to a fraction, f, of its initial value. Comparing different inlet stoichiometries (C/O ratios) shows that they all have the same initial velocities but different gas temperature profiles (see Fig. 4). However, the overall temperature dependence of z is weak, only $\sim\overline{T}^{0.3}$, as $\bar{u}\sim\overline{T}$ and $\overline{k_{O_2}^m}\sim\overline{T}^{1.3}$ [28]. Therefore, the right side of Eq. (12) is about the same for each C/O ratio. This means that if the rate of O_2 consumption is determined by mass transport, then a given value of f should be reached at about the same axial coordinate, z. On the other hand, if mass transport and O_2 consumption on the surface are comparable in rate ($Y_{O_2}^s = Y_{O_2}^s(z) > 0$), then Eq. (10) would have to be integrated, and the axial coordinate z, at which a given value f is reached, would be different for each C/O ratio.

The ratio of the O_2 mass fractions $f = Y_{O_2}^{bz}/Y_{O_2}^{bin}$ is the same as the ratio of the corresponding O_2 molar flow rates $f = F_{O_2}^{bz}/F_{O_2}^{bin}$. For our analysis in Fig. 7, we chose the points at which the O_2 flow rates reach 50% of their inlet values ($f = F_{O_2}^{bz}/F_{O_2}^{bin} = 0.5$) or nearly zero (end oxidation zone, $f \to 0$) to verify whether the methane CPO is fully O_2 mass transport-controlled on Rh and Pt or whether surface reactions and mass transport are comparable in rate. On Rh, the reaction is fully oxygen mass transport-controlled in the middle of the oxidation zone ($f = 0.5$) and toward the end. The axial positions at which these points are reached are nearly independent of the C/O ratio.

3.4.3. Kinetic control on Pt

On Pt, the axial coordinate for $f = 0.5$ depends linearly on the concentration. This indicates a constant reaction rate in the oxidation zone, independent of the inlet stoichiometry. Equation (13) calculates the corresponding O_2 mass balance with r in $\mathrm{mol/m^3/s}$ as the reaction rate and W_{O_2} the molecular weight of oxygen in kg/mol:

$$\rho u\frac{\mathrm{d}Y_{O_2}^b}{\mathrm{d}z} = -r\cdot W_{O_2}. \qquad (13)$$

Introduction of $f = Y_{O_2}^{bz}/Y_{O_2}^{bin} = F_{O_2}^{bz}/F_{O_2}^{bin}$ and integration from 0 to z yields the equation:

$$z = Y_{O_2}^{bin}\cdot(1-f)\cdot\frac{\rho u}{r\cdot W_{O_2}}, \qquad (14)$$

which shows that for a given f (e.g., 0.5), z increases linearly with $Y_{O_2}^{bin}$ and $z = 0$ for $Y_{O_2}^{bin} = 0$. Both is observed in Fig. 7.

A possible explanation for the constant reaction rate in the oxidation zone on Pt would be that only few surface sites are available for reaction, making the reaction rate largely independent of the reactant concentrations in the gas phase. In fact, numerical simulations predict high carbon coverage in the oxidation zone on Pt [5] in line with this interpretation. Toward the end of the oxidation zone, gas-phase O_2 becomes depleted and mass transport rate-limiting. Therefore, as predicted by Eq. (12), the profiles on Pt also share a common point of total O_2 conversion.

3.4.4. Oxygen mass transport coefficient

A numerical simulation of the species profiles in the foam requires that the mass transport coefficients be known. Because of the importance of foam catalysts for short contact time reactions, correlations for the Sh number in dependence of Re and Sc number have been established by Giani et al. [28] for pore dimensions of 1–5 mm ($\mathrm{Sh} = 1.1\mathrm{Re}^{0.43}\mathrm{Sc}^{1/3}$). Fig. 8 shows an electron micrograph of a typical pore of our 80 ppi foam. Here the pores are smaller with a diameter around 500 µm. By applying Eq. (12) to our O_2 profiles measured on Rh, we can now calculate an average oxygen mass transport coefficient $\overline{k_{O_2}^m}$ for our foam and compare it to a value from the correlation [28]

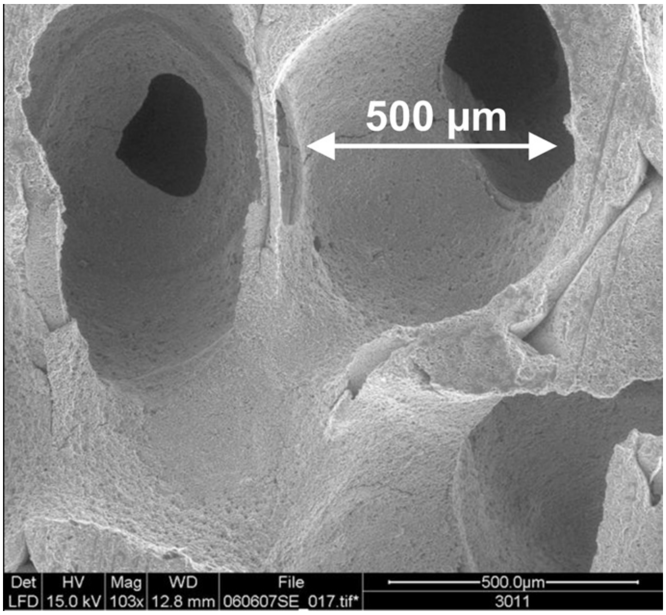

Fig. 8. Electron micrograph of a typical pore in an 80 ppi α-Al_2O_3 foam.

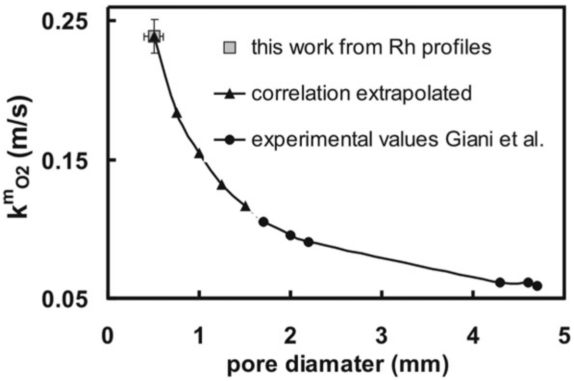

Fig. 9. Comparison of $\overline{k^m_{O_2}}$ calculated from O_2 profiles on Rh (Fig. 7, left), with the correlation $Sh = 1.1Re^{0.43}Sc^{1/3}$ [28] extrapolated to 0.5 mm pore diameter.

extrapolated to our smaller pore size. Re and Sc number are calculated according to our experiment. Fig. 9 shows how strongly the mass transport coefficient increases with decreasing pore diameter and demonstrates that the $\overline{k^m_{O_2}}$ extracted from the profiles on Rh is in excellent agreement with the extrapolated correlation from Giani et al. [28].

3.5. Comparison with thermodynamic equilibrium calculations

As a last point in the comparison of Rh and Pt as catalysts for the methane CPO, in this section we discuss how closely to thermodynamic equilibrium the reaction is brought by each metal. This question is of high practical relevance, because the upper yields of the target molecules H_2 and CO are limited only by thermodynamic equilibrium. This is in contrast to most other partial oxidations, in which the target molecules essentially do not exist at thermodynamic equilibrium.

The reactor described in Section 2.2 operates in good approximation adiabatically; thus, equilibrium is calculated for constant pressure (101.325 kPa) and enthalpy. The Equil program [29] in the CHEMKIN software package has been used to perform these calculations. The flow rates of the different species measured at the end of each catalyst and the calculated equilibrium values are compared in Fig. 10.

3.5.1. Equilibrium values

Equilibrium O_2 conversion is 100% for all C/O ratios investigated ($F_{O_2} = 0$ mol min^{-1}). CH_4 conversion is incomplete ($F_{CH_4} > 0$ mol min^{-1}) if C/O $\geqslant 0.8$. The equilibrium molar flow rates of H_2 and CO increase with decreasing C/O ratio, reaching maximums of about 0.095 mol min^{-1} and 0.045 mol min^{-1}, respectively, at C/O = 0.9. Even lower C/O ratios (i.e., higher O_2 concentrations) lead to enhanced total oxidation with an increasing H_2O flow rate and decreasing H_2 and CO flow rates. The equilibrium CO_2 flow rate is small because the exothermic water–gas shift reaction (Eq. (15)) is far to the left side. The equilibrium CO_2 flow rate rises somewhat toward higher C/O ratios as the temperature decreases.

$$CO + H_2O \rightleftharpoons CO_2 + H_2, \quad \Delta H_r^\circ = -41 \text{ kJ mol}^{-1}. \tag{15}$$

The equilibrium temperature is lowest at C/O = 2.6 and increases only slowly from 575 °C at C/O = 2.6 to 719 °C at C/O = 0.9. At lower C/O ratios, the equilibrium temperature rises sharply up to 1317 °C (C/O = 0.6) due to the increasing amount of H_2O formation.

3.5.2. Experimental exit values

Qualitatively, the experimental flow rates at the exit of each catalyst follow the thermodynamic trends. Independent of C/O, both metals achieve complete O_2 conversion within the first few mm (Fig. 4). For all other species there, distinct quantitative differences between Rh and Pt can be seen.

Rh is generally the more active and more selective catalyst for methane CPO. Up to C/O = 1.0, the exit CH_4 flow rate is only slightly higher than the equilibrium curve on Rh but significantly higher than the curve on Pt. This again reflects the fact that Rh is a much more active steam-reforming catalyst than Pt.

Also straightforward is the interpretation of the exit CO_2 flow rates. As mentioned earlier, CO_2 equilibrium is governed by the water–gas shift reaction (Eq. (15)). On both metals the CO_2 flow rate is below equilibrium, and the distance to equilibrium increases with falling catalyst temperature (increasing C/O). Close inspection shows that the CO_2 flow rate is lower on Rh than on Pt. This indicates that there is some kinetic control on CO_2 formation in the oxidation zone. Rh forms less CO_2 than Pt in favor of CO, especially at high C/O ratios. The water–gas shift equilibrium is approached only at very high catalyst temperatures (C/O = 0.6, 0.7).

The exit flow rates of H_2, CO, and H_2O are governed not only by the extent of steam reforming, but also by the extent of the water–gas shift. As equilibrium of Eq. (15) is not fully established; on both metals, the exit CO flow rates are closer to the equilibrium curve than H_2 or H_2O.

The exit H_2 flow rates on Rh follow the equilibrium curve closely for C/O $\leqslant 1.0$. At low C/O, Rh achieves H_2 flow rates

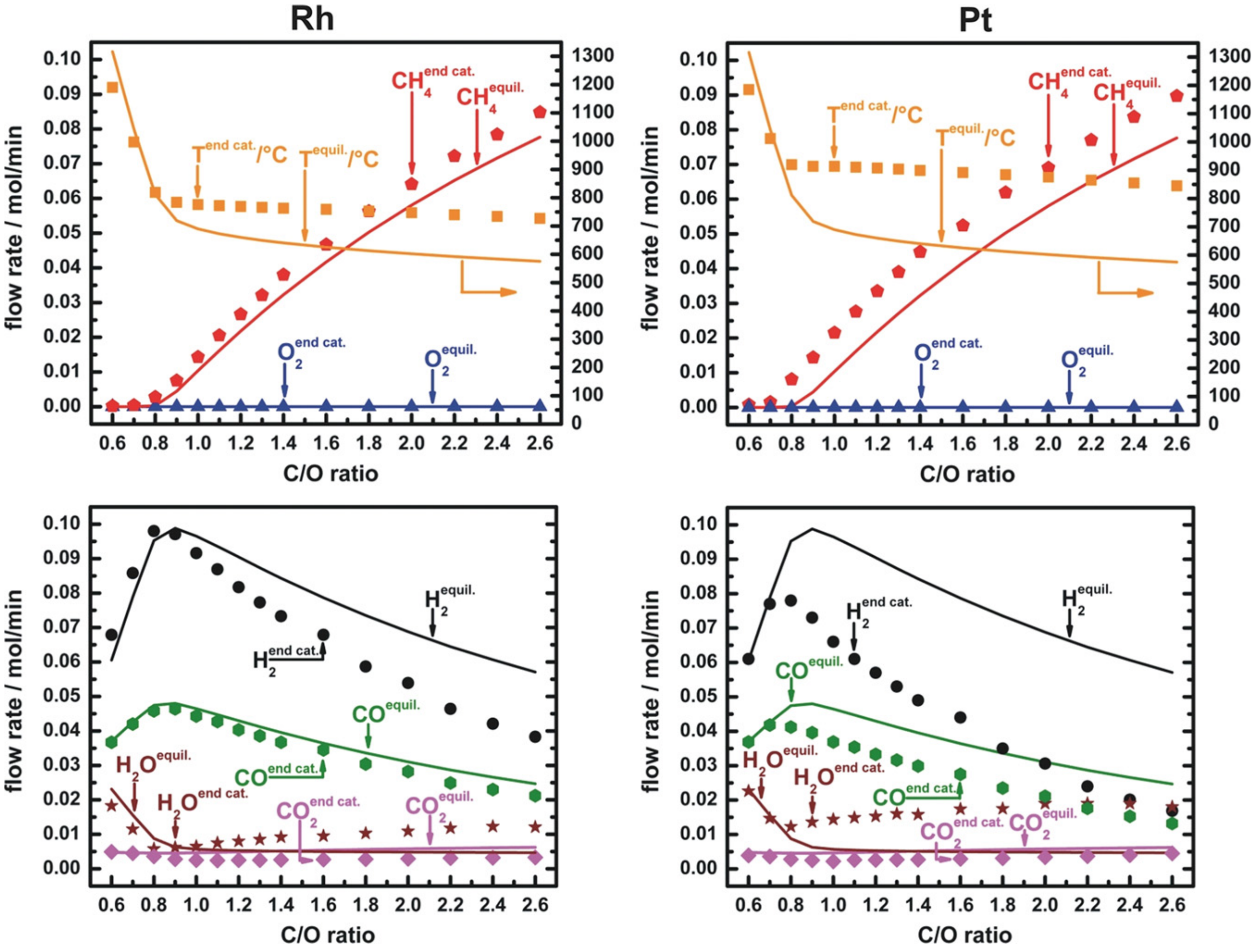

Fig. 10. Comparison of experimental exit flow rates and exit temperatures (symbols) with values at thermodynamic equilibrium (p, H = const., lines).

even slightly higher than thermodynamic equilibrium, pointing to a kinetically preferred H_2 formation. The exit H_2 flow rate on Pt reaches equilibrium only if the catalyst temperature is very high, as for C/O = 0.6 and 0.7. At higher C/O, steam reforming on Pt slows rapidly, leading to H_2 exit flow rates far below the thermodynamic limit. Steam reforming on Rh slows less rapidly, leading to exit H_2 flow rates closer to the thermodynamic limit.

4. Conclusions

This work compares Rh and Pt as catalysts for the catalytic partial oxidation of methane by investigating species and temperature profiles measured along the centerline of an adiabatically operated foam coated with the metal.

On both metals, a short oxidation zone forms at the catalyst entrance, followed by a longer steam-reforming zone. The oxidation zone is longer on Pt than on Rh. H_2 and CO are formed by partial oxidation and by steam reforming. CO_2 reforming is not observed.

The product selectivities and yields in the oxidation zone are strongly temperature-dependent. High temperatures (i.e., low C/O) favor partial oxidation to H_2 and CO, and low temperatures (i.e., high C/O) favor total oxidation to H_2O and CO_2. Rh has generally a higher selectivity and provides higher yields of H_2 and CO than Pt. The different catalytic behaviors can be understood in terms of different activation barriers for the formation of OH and the redissociation of CO_2 on each metal surface [1]. In addition, the O_2 profiles on Rh and Pt show that the reaction is largely mass transport-controlled in the oxidation zone on Rh but kinetically controlled on Pt. O_2 mass transport limitations are another reason for the better performance of Rh as partial oxidation catalyst.

Another important difference between Rh and Pt is that Rh catalyzes steam reforming much more efficiently than Pt. Steam reforming is much slower on Pt than on Rh, leading to below-equilibrium selectivities of H_2 and CO and above-equilibrium selectivities of H_2O for $C/O \geqslant 0.8$. Rh follows the equilibrium curve up to C/O = 1.0. The lower extent of endothermic steam reforming leads to higher exit temperatures on Pt than on Rh.

Acknowledgments

R. Horn gratefully acknowledges funding through an Alexander von Humboldt Foundation Feodor Lynen Fellowship. Financial support also was provided by the Department of Energy (grant DE-FG36-05GO15023). The authors thank Michael Geske and Katrin Pelzer from the Fritz-Haber-Institute of the

Max-Planck-Society/Berlin for placing the electron micrograph shown in Fig. 8 at our disposal.

References

[1] D.A. Hickman, L.D. Schmidt, Science 259 (1993) 343.
[2] S.C. Reyes, J.H. Sinfelt, J.S. Feeley, Ind. Eng. Chem. Res. 42 (2003) 1588.
[3] A.P.E. Yorck, T. Xiao, M.L.H. Green, Top. Catal. 22 (2003) 345.
[4] D. Wolf, M. Hoehenberger, M. Baerns, Ind. Eng. Chem. Res. 36 (1997) 3345.
[5] O. Deutschmann, L.D. Schmidt, AIChE J. 44 (1998) 2465.
[6] C.T. Goralski, R.P. O'Connor, L.D. Schmidt, Chem. Eng. Sci. 55 (2000) 1357.
[7] G. Veser, J. Fraunhammer, Chem. Eng. Sci. 55 (2000) 2271.
[8] O. Deutschmann, R. Schwiedernoch, L.I. Maier, D. Chatterjee, Stud. Surf. Sci. Catal. 136 (2001) 251.
[9] I. Tavazzi, A. Beretta, G. Groppi, P. Forzatti, J. Catal. 241 (2006) 1.
[10] D. Wang, O. Dewaele, A.M. De Groote, G.F. Froment, J. Catal. 159 (1996) 418.
[11] E.P.J. Mallens, J.H.B.J. Hoebink, G.B. Marin, J. Catal. 167 (1997) 43.
[12] H. Heitnes Hofstad, J.H.B.J. Hoebink, A. Holmen, G.B. Marin, Catal. Today 40 (1998) 157.
[13] J.C. Slaa, R.J. Berger, G.B. Marin, Catal. Lett. 43 (1997) 63.
[14] M.M.V.M. Souza, M. Schmal, Appl. Catal. A Gen. 281 (2005) 19.
[15] W.Z. Weng, M.S. Chen, Q.G. Yan, T.H. Wu, Z.S. Chao, Y.Y. Liao, H.L. Wan, Catal. Today 63 (2000) 317.
[16] M. Lyubovsky, S. Roychoudhury, R. LaPierre, Catal. Lett. 99 (2005) 113.
[17] R. Horn, K.A. Williams, N.J. Degenstein, L.D. Schmidt, J. Catal. 242 (2006) 92.
[18] R. Horn, N.J. Degenstein, K.A. Williams, L.D. Schmidt, Catal. Lett. 110 (2006) 169.
[19] R. Horn, K.A. Williams, N.J. Degenstein, L.D. Schmidt, Chem. Eng. Sci. 62 (2007) 1298.
[20] A.B. Mhadeshwar, D.G. Vlachos, J. Phys. Chem. B 109 (2005) 16819.
[21] J.-D. Grundwaldt, A. Baiker, Catal. Lett. 99 (2005) 5.
[22] J.-D. Grundwaldt, S. Hannemann, C.G. Schroer, A. Baiker, J. Phys. Chem. B 110 (2006) 8674.
[23] N.J. Degenstein, R. Subramanian, L.D. Schmidt, Appl. Catal. A Gen. 305 (2006) 146.
[24] M. Bizzi, L. Basini, G. Saracco, V. Specchia, Chem. Eng. J. 90 (2002) 97.
[25] M. Bizzi, L. Basini, G. Saracco, V. Specchia, Ind. Eng. Chem. Res. 42 (2003) 62.
[26] M. Bizzi, G. Saracco, R. Schwiedernoch, O. Deutschmann, AIChE J. 50 (2004) 1289.
[27] M. Maestri, A. Beretta, G. Groppi, E. Tronconi, P. Forzatti, Catal. Today 105 (2005) 709.
[28] L. Giani, G. Groppi, E. Tronconi, Ind. Eng. Chem. Res. 44 (2005) 4993.
[29] R.J. Kee, F.M. Rupley, J.A. Miller, M.E. Coltrin, J.F. Grcar, E. Meeks, H.K. Moffat, A.E. Lutz, G. Dixon-Lewis, M.D. Smooke, J. Warnatz, G.H. Evans, R.S. Larson, R.E. Mitchell, L.R. Petzold, W.C. Reynolds, M. Caracotsios, W.E. Stewart, P. Glarborg, C. Wang, O. Adigun, W.G. Houf, C.P. Chou, S.F. Miller, CHEMKIN Collection Release 3.7.1 (2003), Reaction Design Inc., San Diego, CA.